


## Skyrmion clusters and chains in bulk and thin-layered cubic helimagnets

Andrey O. Leonov\*

*Department of Chemistry, Faculty of Science, Hiroshima University Kagamiyama, Higashi Hiroshima, Hiroshima 739-8526, Japan  
and IFW Dresden, Postfach 270016, D-01171 Dresden, Germany*

 (Received 12 December 2021; revised 5 February 2022; accepted 11 February 2022; published 2 March 2022)

I overview the properties of nonaxisymmetric isolated skyrmions (ISs), which arise within a cone phase of cubic helimagnets. The nascent conical state is shown to shape skyrmion internal structure and to substantiate the attracting skyrmion-skyrmion interaction. In bulk cubic helimagnets, skyrmion cluster formation with the hexagonal arrangement of constituent skyrmions is explained by the reduction of the total energy due to the overlap of skyrmion shells—circular domain boundaries with the positive energy density formed with respect to the surrounding host phase. In thin layers, however, such a shell localizes within two bags on the opposite sides from the skyrmion cores, which underlies the formation of polar skyrmion chains with the most effective suppression of the shell energy. A systematic analysis of skyrmion trio-clusters and trio-chains reveals that their thickness-dependent advantage rests on a subtle energetic balance between the “lost” negative energy of the skyrmion rings and the “gained” energy due to the suppressed shells. Such a polar ordering of nonaxisymmetric skyrmions was recently observed within the “schools” of liquid-crystal skyrmions powered into motion by an applied electric field [*Nat. Commun.* **10**, 4744 (2019)]. Thus, the fundamental insights provided by this work imply deep physical relations and common physical features of skyrmions in different condensed-matter systems such as chiral liquid crystals and chiral magnets.

DOI: [10.1103/PhysRevB.105.094404](https://doi.org/10.1103/PhysRevB.105.094404)

### I. INTRODUCTION

Isolated chiral skyrmions [1–3] are smooth, topological, and static spin textures stabilized in noncentrosymmetric magnetic materials by a specific Dzyaloshinskii-Moriya interaction (DMI) [4,5]. Phenomenologically, DMI is expressed by the energy terms containing the first derivatives of the magnetization  $\mathbf{M}$  with respect to the spatial coordinates, so called Lifshitz invariants (LIs):

$$\mathcal{L}_{i,j}^{(k)} = M_i \partial M_j / \partial x_k - M_j \partial M_i / \partial x_k. \quad (1)$$

These LIs arise in certain combinations depending on the crystal symmetry of an underlying chiral magnet. Moreover, they lead to a unique internal structure of isolated skyrmions (ISs) by defining their vorticity and helicity [1]. For cubic helimagnets belonging to 23 (T) (such as MnSi [6], FeGe [7], and other B20 compounds) and 432 (O) crystallographic classes, Dzyaloshinskii-Moriya interactions are reduced to the following form [1]:

$$W_{\text{DMI}} = D (\mathcal{L}_{yx}^{(z)} + \mathcal{L}_{xz}^{(y)} + \mathcal{L}_{zy}^{(x)}) = D \mathbf{M} \cdot \text{rot} \mathbf{M}, \quad (2)$$

which leads to Bloch-type skyrmions.

The relevant lengthscale of a magnetic inhomogeneity squeezed into a skyrmionic knot is tuned by the competition between this chiral and direct exchange [1,8]. Moreover, DMI provides a unique stabilization mechanism, protecting skyrmions from radial instability and overcoming the

constraints of the Hobart-Derrick theorem [9]. Due to the nanometer size, topological protection, and the ease with which skyrmions can be manipulated by electric currents, the magnetic skyrmions are considered as promising objects for the next-generation memory and logic devices. In particular, in the skyrmion racetrack [10–12], information flow is encoded in isolated skyrmions [13] moving within a narrow strip.

Skyrmionic “particles” may also be driven together to form complex noncollinear magnetic textures—skyrmion lattices (SkLs) [14,15], clusters [16,17], or even skyrmion superstructures composed from mutually orthogonal skyrmion tubes, which involve so called horizontal skyrmions [18]. The formation of these textures is determined by the stability of the localized solitonic cores, their geometrical incompatibility that frustrates homogeneous space-filling, and the tendency to reduce their own energy. Versatile skyrmion conglomerates might further extend the functionalities and underlie a novel concept of spintronic devices based, e.g., on gapless skyrmion motion along each other [18]. Alternatively, the density of topologically encoded information could be increased by using densely packed and well-distinguished skyrmion superstructures. In this sense, one could also mention composite skyrmion bags—multiple skyrmions surrounded by a circular spiral state [19,20].

The energy contributions phenomenologically analogous to the DMI also arise in chiral liquid crystals [21,22], and they are rooted in the acentric shape of underlying molecules. Studies of different naturally occurring and/or laser-generated topological objects began in chiral liquid crystals (CLCs)

\*leonov@hiroshima-u.ac.jp

[23–25] long before magnetic skyrmions attracted a great deal of attention in chiral magnets (ChMs). In particular, the above-mentioned horizontal skyrmions [18] have long been known in the physics of CLCs as Lehmann clusters [26]. Nowadays, CLCs are considered to be highly accessible model systems [27] for probing the behavior and topology of various three-dimensional (3D) knotted structures even with singular field configurations such as torons [28].

Topologically, skyrmions are elements of the second homotopy group [19]  $\pi_2(\mathbb{S}^2) = \mathbb{Z}$ , and they represent smooth and topologically nontrivial structures in the alignment field of constituent rodlike molecules, the director field  $\mathbf{n}(\mathbf{r})$ , or the magnetization  $\mathbf{M}(\mathbf{r})$ . They are characterized by integer-valued topological invariants, i.e., the skyrmion numbers  $Q$  [2,19], which also indicate that skyrmions cannot be continuously morphed into a homogeneous state without introducing point defects [29].  $Q = \frac{1}{4\pi} \int \mathbf{m}(\frac{\partial \mathbf{m}}{\partial x} \times \frac{\partial \mathbf{m}}{\partial y}) dx dy$ . I notice, however, that in CLCs, nonpolar skyrmions are represented by the homotopy group  $\pi_2(\mathbb{S}^2/\mathbb{Z}_2) = \mathbb{Z}$  and wrap around the order parameter space ( $\mathbb{S}^2/\mathbb{Z}_2$ ) twice. But being vectorized, the director field becomes analogous to the magnetization field, although the topological charge in this case can be defined only up to the sign [27]. Remarkably, in CLC layers with thickness slightly smaller than the spiral pitch, skyrmions were shown to cohere into single-file lines or chains—another type of skyrmion conglomerate. By using ambient-intensity unstructured light, the authors of Refs. [30,31] demonstrated large-scale multifaceted transformations between such chains and skyrmion clusters, dubbed skyrmion “schools.”

The promising technological potential offered by ISs and their superstructures at reduced dimensions mainly hinges on the effective use of two key ingredients: (i) chiral surface twists, and (ii) skyrmion-skyrmion interaction.

(i) Due to additional surface twists, skyrmions gain their stability in thin layers of chiral magnets for a broad range of applied out-of-plane magnetic fields and nanolayer thicknesses  $T$  [32,33]. Indeed, in bulk helimagnets only the Lifshitz invariants  $\mathcal{L}_{x,y}^{(x,y)}$  compel the magnetization rotation in the  $xy$  plane. In cubic helimagnets and CLCs, these LIs fix the skyrmion helicity at the value  $\gamma = \pi/2$  (Bloch-like fashion of rotation). In magnetic nanolayers, on the contrary, the LI  $\mathcal{L}_{x,y}^{(z)}$  with the magnetization derivative along  $z$  comes into play. For skyrmions,  $\mathcal{L}_{x,y}^{(z)}$  leads to the gradual change of the skyrmion helicity [ $\gamma = \pi/2 \pm \delta(z)$ ] toward upper and lower surfaces [32,33]. This effect accumulates additional negative energy compared with the cones not decorated by the additional surface twists [32,33], and it leads to the SkL stability (up to the confinement ratio  $\nu = T/\lambda \approx 8$ , where  $\lambda$  is a spiral pitch).

(ii) The character of IS-IS interaction as well as the intricate three-dimensional internal structure of ISs are imposed by a surrounding “parental” state. Being surrounded by the saturated phase, skyrmions acquire an axisymmetric shape and exist as ensembles of weakly repulsive particles [34–36]. The spins in the homogeneous state are parallel and point either to an applied magnetic field or to an easy axis of a uniaxial anisotropy. The detailed behavior of such isolated skyrmions has been reported in PdFe/Ir(111) bilayers with the induced DMI and a relatively high value of the uniaxial anisotropy [36]. On the other hand, being embedded in the cone

phase of chiral ferromagnets, isolated skyrmions acquire a nonaxisymmetric shape, become mutually attractive, and thus tend to produce skyrmion superstructures including clusters and chains [16,17,30,31]. The same regimes of skyrmion interaction are experimentally observed in CLCs [27]. In particular, an analog of the conical phase can be achieved as a result of the competition between the director’s tendency to twist, and the surface anchoring accompanied by the confinement at finite sample thickness [37].

In the present paper, I will examine the principles of IS condensation into skyrmion clusters and skyrmion chains in chiral magnets and liquid crystals. The remainder of the manuscript is organized as follows. In the next section (Sec. II), I introduce a phenomenological model and the algorithms used for simulations. Within the continuum and discrete models under consideration, the applied magnetic field and the film thickness are the only two control parameters. First, I plot the phase diagram of spiral states (Sec. III), which exhibits one-dimensional (1D) conical states, i.e., straight and oblique spirals. I discuss the first- and second-order phase transitions between these modulations. In Sec. IV, I examine the internal structure of IS tubes in bulk cubic helimagnets. I argue that skyrmion trio-clusters in this case represent an energetically favorable configuration as compared with the skyrmion trio-chains. The constructed 3D skyrmion models provide a straightforward explanation of the attractive nature of skyrmion-skyrmion interaction. I further deduce that the process of skyrmion condensation into clusters is ruled by the two competing mechanisms: although skyrmions lose some low energy of skyrmion rings, they effectively eliminate the high-energy edge area in the interskyrmion region, which underlies skyrmion attraction. Finally, I illustrate the process of cluster and chain formation in thin films of chiral magnets (Sec. V) with the energetic advantage of the latter state.

## II. THE MODEL

### A. A continuum energy functional

Within the phenomenological theory introduced by Dzyaloshinskii [5,38], the magnetic energy density of a noncentrosymmetric ferromagnet with spatially dependent magnetization  $\mathbf{m}$  can be written as

$$W(\mathbf{m}) = A (\mathbf{grad} \mathbf{m})^2 + D \mathbf{m} \cdot \text{rot} \mathbf{m} - \mu_0 M \mathbf{m} \cdot \mathbf{H}, \quad (3)$$

where  $A > 0$  and  $D$  are coefficients of exchange and Dzyaloshinskii-Moriya interactions,  $\mathbf{H}$  is an applied magnetic field along the  $z$ -axis, and  $x_i$  are the Cartesian components of the spatial variable. To describe skyrmionic states, I will also use cylindrical coordinates  $(\rho, \varphi)$  for the spatial variable. Moreover, only skyrmions with  $Q = 1$  are thoroughly scrutinized. Functional (3) includes only basic interactions essential to stabilize skyrmion and helical states. The temperature is assumed to be much below the ordering temperature. Then, the order parameter can be presented as a continuous unit-vector field  $\mathbf{m} = (\sin \theta \cos \psi; \sin \theta \sin \psi; \cos \theta)$  along the magnetization vector  $\mathbf{M} = \mathbf{m} M_s$ , where  $M_s$  is the saturation magnetization.

The first two terms in model (3) also correspond to the elastic energy contributions in the Franck free energy of CLCs

that pertain to splay  $K_1$ , twist  $K_2$ , and bend  $K_3$  distortions of the director provided that the one-constant approximation  $K_1 = K_2 = K_3 = K$  is utilized [21,22]:  $A \rightarrow K/2$ ,  $D \rightarrow Kq_0$ . ( $q_0 = 2\pi/\lambda$  is the chiral wave number of the ground-state chiral nematic mixture.) Indeed, the values of elastic constants in common CLCs are comparable, and this one-constant approximation is commonly used. The absence of a Zeeman-like term in CLCs in the elastic (Frank) free energy is compensated by the interplay of the electric field and the surface anchoring. As a result, the CLC conical phase acquires the angle varying across the layer thickness. These arguments facilitate the discussion of topological phases in CLCs and ChMs on the same footing [27,28,39], and similar phenomena and structures can be expected in both condensed-matter systems.

I investigate the functional (3) in a film of thickness  $T$  infinite in the  $x$  and  $y$  directions and confined by parallel planes at  $z = 0; T$ . This means that periodic boundary conditions are applied along  $x$  and  $y$  only, whereas the free boundary conditions are considered at both surfaces. In the modeling of CLCs, surface interactions (e.g., the Rapini-Papoular surface energy density and/or saddle-splay deformations  $K_{24}$ ) often play a crucial role in the stability of modulated states [28,39]. In the present manuscript, however, the surface-induced effects are omitted.

The equilibrium magnetic states within the model (3) have been obtained by a numerical energy minimization procedure using finite-difference discretization on rectangular grids with adjustable grid spacings. The minimization procedure is described in detail in Ref. [40]. The solutions depend on the two control parameters of the model (3), namely the reduced magnetic field  $h = H/H_D$ , and the thickness  $\nu = T/\lambda$ . Here,  $L_D = A/|D|$  is the characteristic length unit of the modulated states. In the following, the spatial coordinates are measured in units of  $L_D$ . The value  $\lambda = 4\pi L_D$  for  $H = 0$  is the *helix period* for bulk helimagnets (e.g., 18 nm for the bulk MnSi).  $\mu_0 H_D = D^2/(AM)$  is the *critical field*. For a conical phase in bulk helimagnets, the saturation field in units of  $H_D$  equals  $h = 0.5$ . At  $H = 0.5H_D$ , the cone phase transforms into the saturated state with  $\theta = 0$  and thus underlies the crossover between two regimes—interskyrmion attraction and repulsion [16]. The equilibrium parameters for the cone phase are expressed in analytical form [38] as

$$\psi_c = \frac{2\pi z}{\lambda}, \quad \cos \theta_c = \frac{2|\mathbf{H}|}{H_D}, \quad (4)$$

where  $z$  is the spatial variable along the applied field.

### B. A classical spin model

To investigate the solutions for nonaxisymmetric skyrmions within the conical phase, I will mainly use the discretized version of Eq. (3):

$$w = J \sum_{\langle i,j \rangle} (\mathbf{S}_i \cdot \mathbf{S}_j) - \sum_i \mathbf{H} \cdot \mathbf{S}_i - D \sum_i (\mathbf{S}_i \times \mathbf{S}_{i+\hat{x}} \cdot \hat{x} + \mathbf{S}_i \times \mathbf{S}_{i+\hat{y}} \cdot \hat{y} + \mathbf{S}_i \times \mathbf{S}_{i+\hat{z}} \cdot \hat{z}). \quad (5)$$

The classical spins of the unit length are placed in the knots of a three-dimensional cubic lattice.  $\langle i, j \rangle$  denotes pairs of nearest-neighbor spins. The minimization scheme remains essentially the same as was introduced for the continuum energy functional and described in Ref. [40]. However, only the energy minimization with respect to the spin orientation takes place. A point  $(x_n, y_n, z_n)$  on a grid is chosen randomly. Then, the spin in the point is rotated without a change of its length. If the energy change associated with such a rotation is negative, the new orientation is kept. Otherwise, it may be accepted probabilistically. In contrast to the continuum model, in which the characteristic spacings  $\Delta_x, \Delta_y, \Delta_z$  are also adjusted to promote energy relaxation, the distance between the points of the discrete numerical grid is considered by convention to be of unit length. In this case, coordinates of the point  $(x_n, y_n, z_n)$  just represent some ordinary numbers showing in which column or string the point is located. In principle, both models are the same, especially for a large characteristic length, since the continuum model is obtained from the discrete one under conditions of smooth magnetization rotation. The discrete model, however, allows us to address spin distributions of a few lattice constants (in particular, those including defects). In the following, the discrete model is used to address skyrmion clusters, whereas the continuum model was used to plot the phase diagram in Fig. 1.

The first term in (5) describes the ferromagnetic nearest-neighbor exchange with  $J < 0$  (in the numerical simulation,  $J = -1$  is used). The DMI constant  $D$  defines the period of modulated structures  $\lambda$  via the following relation:

$$D/J = \tan(2\pi/\lambda). \quad (6)$$

Or vice versa, one chooses the period of the modulations  $\lambda$  for the computing procedures and defines the corresponding value of the DMI constant. Indeed, for a helix  $\mathbf{S}_i = (\cos \theta_i, \sin \theta_i, 0)$  propagating along the  $x$ -axis at zero field ( $\mathbf{H} = \mathbf{0}$ ), model (5) is reduced to

$$w = \sum_i [-J \cos(\theta_i - \theta_{i+\hat{x}}) - D \sin(\theta_i - \theta_{i+\hat{x}})], \quad (7)$$

which yields the equilibrium period  $\lambda = 2\pi / \arctan(D/J)$  ( $\lambda$  is the number of magnetic ions corresponding to  $\Delta\theta = 2\pi$ ). In what follows, the Dzyaloshinskii-Moriya constant is set to 0.2126, which corresponds to one-dimensional modulations with a period of 30 lattice spacings in a zero field [41]. For simulations within the continuous model, the same value of  $\lambda$  is chosen for the discretization schemes. The size of a numerical grid is set to  $300 \times 300 \times T$  (it might be incommensurate as well), which is sufficient to accommodate skyrmion tri-chains and trio-clusters within the conical phase and to take into account all the subtleties of their internal structure. In this case, one may even use free boundary conditions at both planes  $xz$  and  $yz$ , since the edge states [42] formed at the sides of the numerical cube will not intersect with the skyrmion profiles and will not distort their profiles. In some figures, zoomed images of a part of the grid will be used. Then, the

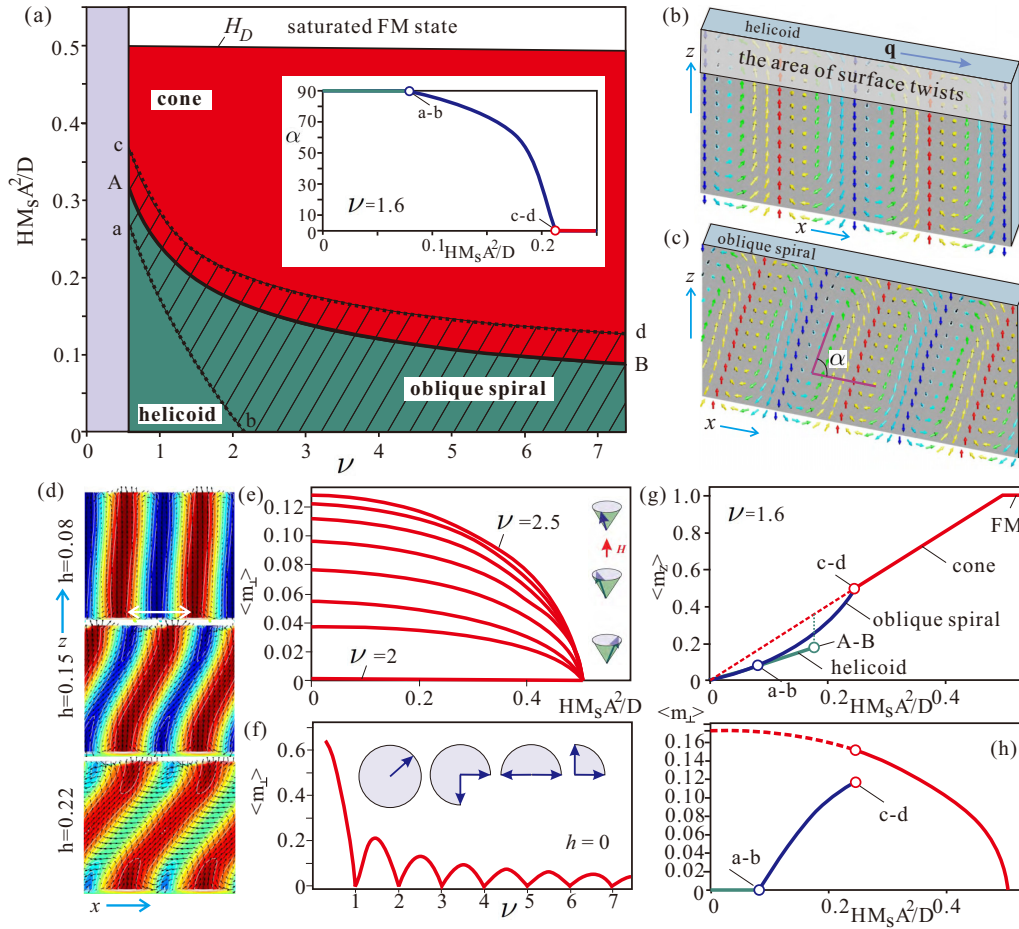


FIG. 1. (a) The magnetic phase diagram of spiral states corresponding to the global minima for model (3) in reduced variables for the film thickness  $\nu = T/4\pi L_D$  and the applied magnetic field  $h = H/H_D$ . Filled areas indicate the regions of global stability for the helicoid (green), cones (red), and oblique spirals (hatched). The white area in (a) designates the ferromagnetic state (FM) fully saturated along the field. The solid line  $A - B$  stands for the first-order phase transition between cones and helicoids, whereas the dotted lines  $a - b$  and  $c - d$  confine the area of the oblique spiral. (b),(c) Magnetic structure of a helicoid (b) with period  $\lambda$  and an oblique spiral in nanolayers of cubic helimagnets. In the surface area, both spirals acquire additional surface twists of the magnetization. (d) The color plots for  $m_z$ -components of the magnetization within an oblique spiral state during its transformation from the helicoid into the conical phase,  $\nu = 1.6$ .  $m_x$  and  $m_z$  components are shown with thin black arrows. The tilt angle  $\alpha$  defined in (c) smoothly varies as shown by the inset in (a). (e) The in-plane component of the magnetization  $\langle m_{\perp} \rangle$  within the conical state in dependence on the field for different ratios  $\nu$ . (f) Oscillations of  $\langle m_{\perp} \rangle$  depending on the film thickness for zero field  $h = 0$ . (g),(h) Magnetization curves for the out-of-plane (g) and in-plane (h) magnetization components demonstrate jumps at the lines of the phase transitions according to the phase diagram in (a).

size of this area will be additionally indicated, for example  $150 \times 150$ . Still, the size of the grid remains the same.

### III. THE PHASE DIAGRAM OF SPIRAL STATES

First of all, I identify the following modulated phases to be included in the phase diagram: helicoids, cones, oblique spirals, and the homogeneous state. Although the skyrmion lattice occupies a vast area of the phase diagram as found by previous studies [33,43], I omit this state in the present consideration. First of all, SkL represents an ideal construct that does not include an energetically costly domain boundary with respect to the conical phase. Moreover, in real experiments, skyrmions undergo nucleation processes: in Ref. [33] in particular, SkL appeared at the edge of a sample and inevitably created a mentioned transient region, which resulted

in much smaller critical film thicknesses  $\nu$  for SkL stability as opposed to the value originally predicted by the theory in the same manuscript. Indeed, already for  $\nu = 1.29$  the skyrmion lattice does not arise; instead, the helicoid directly transforms into the cone phase.

The helicoid [also called a chiral soliton lattice (CSL)] occupies the green-shaded area of the phase diagram [Fig. 1(a)]. The wave vector of CSL lies within the plane  $xy$  (for definiteness, along the  $x$ -axis) [Fig. 1(b)]. For low field values, such spirals have lower energy as compared with the conical state, which is readily explained by the additional surface twists in thin-film nanosystems, i.e., due to the same LIs  $\mathcal{L}_{x,y}^{(z)}$ , which also underlie skyrmion stability. In the same way, whereas the LIs with the derivatives along the  $x$  and  $y$  axes govern the magnetization rotation in spiral states, the LI with the derivative along  $z$  leads to the gradual change of the spiral

helicity toward upper and lower surfaces with the penetration depth  $2\pi L_D$ . This effect accumulates additional negative energy compared with the cones [32,33]. The area of surface twists within the helicoid is schematically shown in Fig. 1(b). Moreover, the surface twists endow such a helicoid with the topological charge: although the total charge calculated in the plane  $xz$  within one spiral period is zero, half-periods of a helicoid bear topological charges  $Q \approx \pm 0.2$  with the opposite signs.

Cones in this geometry [schematically shown in the inset of Fig. 1(e)] are oriented along the field and inhabit the red-shaded region at the phase diagram [Fig. 1(a)]. Since usually the film thickness is a noninteger multiple of the helical wavelength, the magnetization of the cones has an uncompensated value of the in-plane component  $m_\perp$  even in zero magnetic field. Figure 1(e) shows the field dependence of the average value  $\langle m_\perp \rangle$  for the film thickness in the range  $\nu \in [2, 2.5]$ . In zero field [Fig. 1(f)],  $\langle m_\perp \rangle$  oscillates depending on  $\nu$  with the lowering amplitude of the oscillations. This effect provides an additional leverage over, e.g., the orientation of skyrmion clusters and chains within the conical phase, and thus it may impart a correct direction for their current-driven movement in spintronic devices.

Along the line  $A-B$  [Fig. 1(a)], the CSL transforms into the conical state. Since it is the first-order phase transition, it must be accompanied by the coexisting domains of both phases, which are readily resolved experimentally by Lorentz transmission electron microscopy investigations in thin layers of cubic helimagnets, e.g., in FeGe (see Fig. 4 in Ref. [33]). The domain of the conical state nucleates and broadens along the lines of  $m_z = 1$  within the helical state and leads to gradual unzipping and drift of two spiral loops from each other.

Besides, the thin-film geometry permits a stable oblique spiral [Figs. 1(c) and 1(d)], which originates from the interplay between the exchange and rotational DMI energy. Whereas the negative energy associated with the surface twists remains almost unchanged, the canting leads to the lowering of the DMI energy, although with some accompanying increase of the exchange energy. Such an oblique spiral exists in the hatched region of the phase diagram bounded by the lines  $a-b$  and  $c-d$  and thus serves as an intermediate state between cones and helicoids. For  $\nu = 1.6$ , the canting angle of rotational planes gradually changes from  $\alpha = 90^\circ$  in the helicoid to 0 in the conical state [inset of Fig. 1(a)]. Interestingly, being unidentified in experiments on thin layers of chiral helimagnets (although predicted theoretically in Ref. [44] for epitaxial films of MnSi [45]), oblique spirals are known in CLCs under the term ‘‘nonsingular fingers of CF1 type.’’ In Ref. [46] in particular, a periodic finger pattern composed of CF1s was experimentally shown to transform into a conical state called translationally invariant configuration (TIC) with uniform in-plane twist because of the weak in-plane anchoring. The fingers gradually widened and then merged in order to form the modulated TIC.

Experimentally, an oblique spiral state can be identified at the magnetization curves for the magnetization components parallel [Fig. 1(g)] and perpendicular [Fig. 1(h)] to the field. Whereas CSL has zero  $\langle m_\perp \rangle$  and almost linearly increasing  $\langle m_z \rangle$  until it jumps into the conical state, an oblique spiral clearly exhibits a growing  $\langle m_\perp \rangle$ -component with the sign of

derivative opposite to the conical one and a gradually varying  $\langle m_z \rangle$ , which merges with the conical one.

#### IV. ISOLATED SKYRMIONS WITHIN THE CONICAL STATE OF BULK CUBIC HELIMAGNETS

The oblique spiral phase in thin layers represents an interesting environment to accommodate ISs and to shape their intrinsic properties. One may then envision two varieties of mutually orthogonal skyrmions and their field-driven rotation: an isolated skyrmion with its axis along  $z$  within the helical phase would become an IS along  $x$  within the conical phase. Such an intriguing skyrmion reorientation, however, will be considered elsewhere. In the present manuscript, I concentrate exclusively on ISs within the conical state with their axes oriented along the field. In this case, the phase diagram provides some useful information on appropriate control parameters to avoid undesirable skyrmion deformations. Then, I start the analysis from isolated skyrmions in bulk ChMs.

##### A. The nature of skyrmion shells in bulk helimagnets

Below the saturation field [ $H < 0.5H_D$ , Fig. 1(a)], the structure of 2D ISs is imposed by the arrangement of the cone phase (4). I note that the value of the critical field is the same for bulk and thin-film helimagnets, which is explained by the undistorted rotation of the magnetization within the conical phase. Only the energy term  $\mathcal{L}_{x,y}^{(z)}$  stipulates the magnetization rotation within the conical phase with the wave vector along  $z$ .

The skyrmion solutions should then be periodic with the period  $4\pi L_D$  along the  $z$ -axis (although in Ref. [40] it was shown that there is a small deviation from this periodicity meant to reduce the positive energy of metastable skyrmions). Moreover, skyrmions are confined by the following boundary conditions:

$$\theta_{\rho=0} = \pi, \quad \theta_{\rho=\infty} = \theta_c, \quad \psi_{\rho \rightarrow \infty}(z) = \psi_c(z). \quad (8)$$

The solutions for  $\theta(\rho, \varphi, z)$ ,  $\psi(\rho, \varphi, z)$  are derived by minimization of the energy functional (3):

$$w = A\mathcal{J}(\theta, \psi) + D\mathcal{I}(\theta, \psi) - \mu_0 MH \cos \theta, \quad (9)$$

with the boundary conditions (8), where the exchange ( $\mathcal{J}$ ) and Dzyaloshinskii-Moriya ( $\mathcal{I}$ ) energy functionals are [41] as follows:

$$\begin{aligned} \mathcal{J}(\theta, \psi) &= \theta_\rho^2 + \theta_z^2 + \frac{1}{\rho^2} \theta_\varphi^2 + \sin^2 \theta (\psi_\rho^2 + \psi_z^2 + \frac{1}{\rho^2} \psi_\varphi^2), \\ \mathcal{I}(\theta, \psi) &= \sin(\psi - \varphi) (\theta_\rho + \frac{1}{\rho} \sin \theta \cos \theta \psi_\varphi) + \sin^2 \theta \psi_z + \cos(\psi - \varphi) (\frac{1}{\rho} \theta_\varphi + \sin \theta \cos \theta \psi_\rho). \end{aligned}$$

Figure 2 shows the results of numerically minimizing the energy functional (9) for bulk helimagnets with  $\lambda = 30$ . The equilibrium structure of such a nonaxisymmetric skyrmion is reached by the incompatibility of the axisymmetric skyrmion core with the transversely modulated cone phase. The asymmetry of skyrmions within the conical phase is clear in both the in-plane (shown as black arrows) and  $z$  components (color plots) of the magnetization. Figure 2(a) (upper panel) shows the magnetization in a plane normal to the direction of the applied field  $z$ . It can be seen that these skyrmions consist of

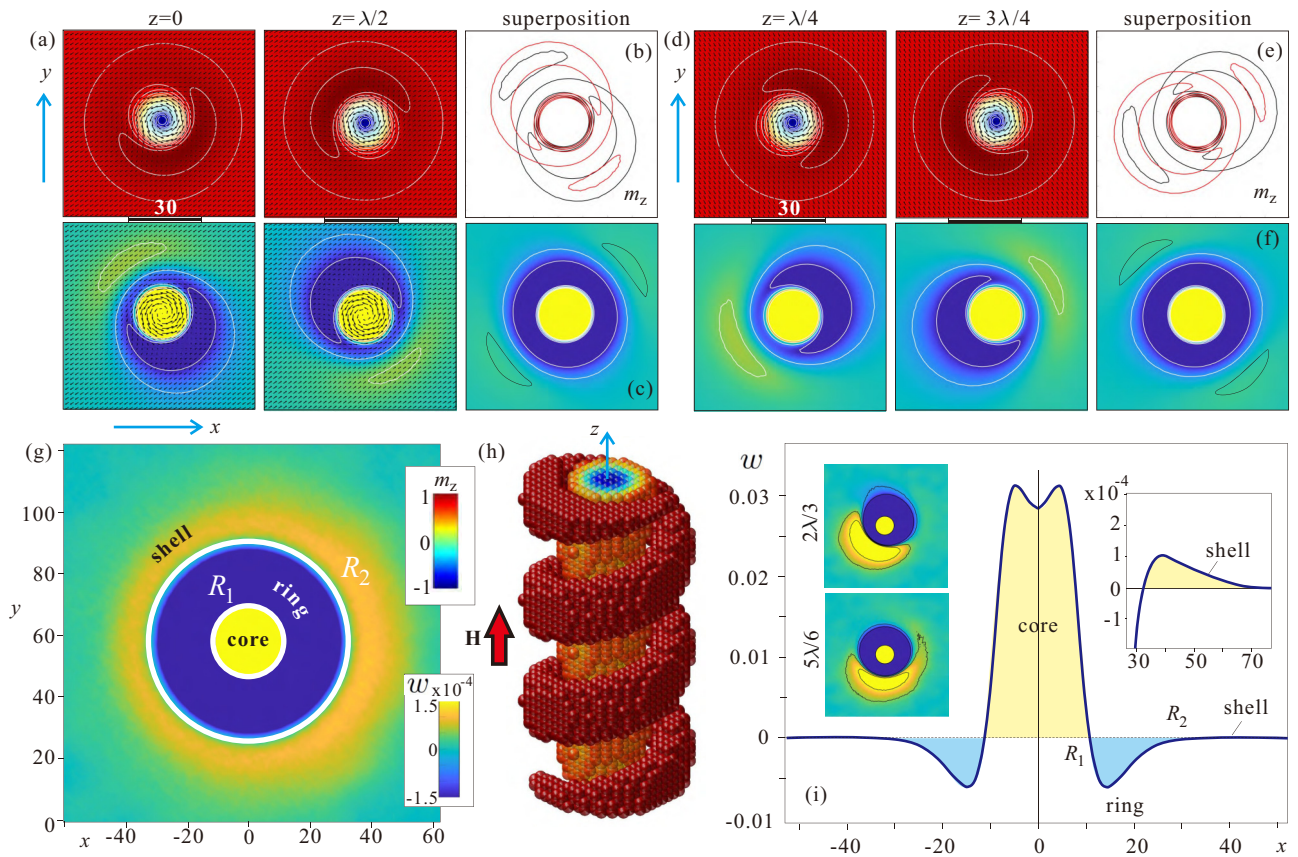


FIG. 2. Magnetic structure of nonaxisymmetric skyrmions within the conical phase of bulk cubic helimagnets. The upper panels in (a) and (d) show color plots of the out-of-plane magnetic moment,  $m_z(x, y)$ . Two skyrmion profiles are located at the distance  $\lambda/2$  from each other. The lower panels in (a) and (d) show corresponding energy density distribution in an  $xy$  plane with a fixed value of  $\psi_c$  (8). Superposition of these profiles correspondingly shown in (b) and (e) lead to the energy profiles shown in (c) and (f). After averaging over all energy profiles within one conical period, the energy distribution (g) exhibits the following composite parts: the core with the positive energy density, the ring with the negative energy density, and the shell with the small positive energy. Since in (g) the range of the energy density is restricted by small values to make the shell region visible, panel (i) shows the crosscut of the energy pattern with the relative heights of all composite parts. Insets in (i) show energy density distributions averaged over  $2\lambda/3$  and  $5\lambda/6$ . In (h), I use an alternative way of representing the internal structure of a nonaxisymmetric skyrmion. After I extracted the magnetization components corresponding to the conical phase, the skyrmion represents a cylinderlike core centered around the magnetization opposite to the field and a coil with the magnetization along the field.

a nearly axisymmetric core surrounded by a crescent-shaped transitional region. The structure shown in (a) gradually rotates on moving along  $z$  from one plane to the next, and two crosscuts in (a) are located at the distance  $\lambda/2$  from each other. The lower panel in Fig. 2(a) shows corresponding energy density distributions. I note that the lowest energy density is reached along the line connecting the skyrmion center with the center of a crescent, where the magnetization passes through the state  $\theta = 0$  and only then tilts to satisfy the boundary conditions (8). Along the opposite direction, the magnetization immediately rotates to the magnetization within the conical phase  $\theta_c$  and thus stipulates the regions with reduced rotational energy [yellow parts in the lower panels of (a) and (d)]. The skyrmion center, i.e., the point at which  $m_z = -1$ , circumscribes a circle around the  $z$  axis. This leads to a nontrivial superposition of energy profiles in Fig. 2(a), as depicted in Figs. 2(b) and 2(c). Only small regions of residual

positive energy density are preserved and located perpendicular to the original crescent parts. The same process occurs for all energy profiles located at the distance  $\lambda/2$  [Figs. 2(d)–2(f)].

Figure 2(g) shows the energy density averaged over all energy profiles within one conical period and plotted on the  $xy$  plane. The zero level is the energy within the conical phase. The characteristic lengths  $R_1$  and  $R_2$  indicate several distinct regions in these radial energy profiles. The positive energy of the “core” is located around the skyrmion center ( $\rho < R_1$ ) and is encompassed by the extended ring area with negative energy density, where the DM coupling dominates ( $R_1 < \rho < R_2$ ) [8]. Within the homogeneous state with the negative asymptotics of the radial energy densities, ISs develop *repulsive* intersoliton potential as originally described in Ref. [8]. In the present case of nonaxisymmetric skyrmions, however, the energy density is positive at large distances from the skyrmion center [Fig. 2(i) and the inset]. This constituent

part of a skyrmion was dubbed “shell” ( $R_2 < \rho$ ) in previous works [41]. The shell separates the skyrmion core from the cone phase. As described before, such a shell must not be visualized as a part of an individual skyrmion cross-section [like those in Fig. 2(a)] that circumscribes a circle and forms a ring with the positive energy density. The shell is rather a result of the superposition of skyrmion profiles when the negative crescent in one cross-section overlaps with the positive energy of a skyrmion profile in a cross-section at the distance  $\lambda/2$  [Figs. 2(c) and 2(f)]. Then, the shell is a part with positive energy, which was left after the superposition. Interestingly, if some energy profiles lack their counterparts for the effective superposition [as described in Fig. 2(a)], which is the obvious case in thin films, the average energy profiles acquire an “out-of-balance” pattern. The color plots shown in the inset of Fig. 2(i) are averaged over the length  $2\lambda/3$  and  $5\lambda/6$ , correspondingly.

A convenient way to depict these skyrmions, which has been proven to be particularly illustrative in addressing the character of skyrmion-skyrmion interaction, is as follows [Fig. 2(h)]: we extract the spins corresponding to the conical phase and then plot the remaining spins as spheres colored according to their  $m_z$ -component. In this way, all intricate details of the internal structure are explicitly revealed, which eliminates the difficulties of plotting skyrmion crosscuts along the different directions. In such a fashion, ISs are composed of a cylinderlike (blue) core centered around the magnetization opposite to the field and a (red) coil with the magnetization along the field [Fig. 2(h)]. From the previous discussion, it becomes clear that the coils bear favorable rotational energy and are associated with crescents in skyrmion crosscuts [Fig. 2(a)], whereas the voids are energetically “handicapped.” Current experimental endeavors are particularly focused on unveiling the three-dimensional spin texture of skyrmion tubes [47–50].

## B. Skyrmion clusters and chains for bulk helimagnets

The positive energy density of the shell underlies attractive interaction between nonaxisymmetric skyrmions [41] and consequently the formation of skyrmion clusters. The color plots in Figs. 3(a)–3(c) indicate the energy density counted from the conical state and plotted on the  $xy$  plane for three configurations: noninteracting isolated skyrmions, skyrmion trio-clusters [composed of three skyrmions (b)], and skyrmion trio-chains (c). Both skyrmion clusters and chains are formed as compromised configurations trying to “cut down” on the positive energy within the shells, but at the expense of the negative energy stored within the rings and inevitably being lost within the intersecting regions [hatched regions in Figs. 3(b) and 3(c)]. As an initial state for minimization procedures, I considered a spin configuration with three isolated skyrmions [Fig. 3(a)] brought into proximity to each other with the subsequent energy minimization.

The table in Fig. 3 shows that skyrmion chains manage to essentially reduce the shell energy  $\Delta E_{\text{shell}}$  (by almost 63% as compared with isolated skyrmions). However, the sacrifice done by the ring energy  $\Delta E_{\text{ring}}$  is higher than that achieved in skyrmion clusters. Moreover, clusters allow the shell energy to be reduced even further (65%). One may conclude that

for bulk helimagnets, skyrmion clusters with a hexagonal arrangement of constituent skyrmions are the most energetically favorable configuration. Since in bulk helimagnets within the isotropic model (5), isolated skyrmions represent metastable particles (i.e., skyrmions have positive total energy over the energy of the conical state, see the table in Fig. 3), cluster and chain formation allows this energy to be reduced. Importantly, the interplay between described “lost”  $\Delta E_{\text{ring}}$  and “gained”  $\Delta E_{\text{shell}}$  energies determines the material parameters of the cluster such as the bound energy and the distance between the constituent skyrmions, which appears to be field-dependent [16,41]. I admit, however, that additional study must address clusters and chains with higher numbers of skyrmions, since other factors (e.g., linear extension of the shell around clusters, or meandering of skyrmion chains) may come into play.

The cluster formation from ISs may alternatively be addressed as a process of zipping skyrmion loops: a coil of one skyrmion penetrates the voids between the coils of another one [Fig. 3(e)]. By this, the lack of rotational energy within the voids (as described in Sec. IV A) is fixed, and the compact skyrmion pair recreates a fragment of a SkL that within the model (3) is a metastable state. The magnetization on the way from the center of one skyrmion to the center of another rotates as in ordinary axisymmetric skyrmions. Such a method, however, does not give a clear indication of which skyrmion arrangement within a cluster is more favorable, and therefore additional energy comparison is vital. Experimentally, skyrmion clusters have been observed in thin (70 nm) single-crystal samples of  $\text{Cu}_2\text{OSeO}_3$  taken using transmission electron microscopy [16] and in nematic fluids, where they were shown to also form skyrmion chains [30,37].

The described mechanism of cluster formation from skyrmions within the conical phase is drastically different from a corresponding mechanism of SkL formation from skyrmions within the homogeneous state (which occurs, e.g., when the conical phase is suppressed by the uniaxial anisotropy, but helicoids and skyrmions still exist as modulated states; see a phase diagram in Ref. [51]). For SkL, the process of condensation is ruled by two competing mechanisms: the total energy of isolated skyrmions (i.e., the sum of the core and the ring energy, since the energy of the shell in this case is zero) becomes negative with respect to the homogeneous state, and skyrmions tend to condense into the hexagonal lattice. However, the energy density becomes larger at the outskirts of the skyrmion, which is the consequence of an inherent frustration built into models with chiral couplings: the system cannot fill the whole space with the ideal, energetically most favored double-twisted motifs. Thus, some loss of the negative ring energy is an aftermath.

The transformation of skyrmions during the formation of the lattice has been investigated in Ref. [8]. Magnetic-field-driven evolution of the skyrmion lattice has similar features with the evolution of helical states investigated in Ref. [5] and bubble and stripe domain in uniaxial ferromagnets [52]. Despite a strong variation of the lattice periods, isolated skyrmions preserve axisymmetric distribution of the magnetization in the central part of cells. The mechanism of lattice formation through nucleation and condensation of isolated axisymmetric skyrmions follows a classification introduced

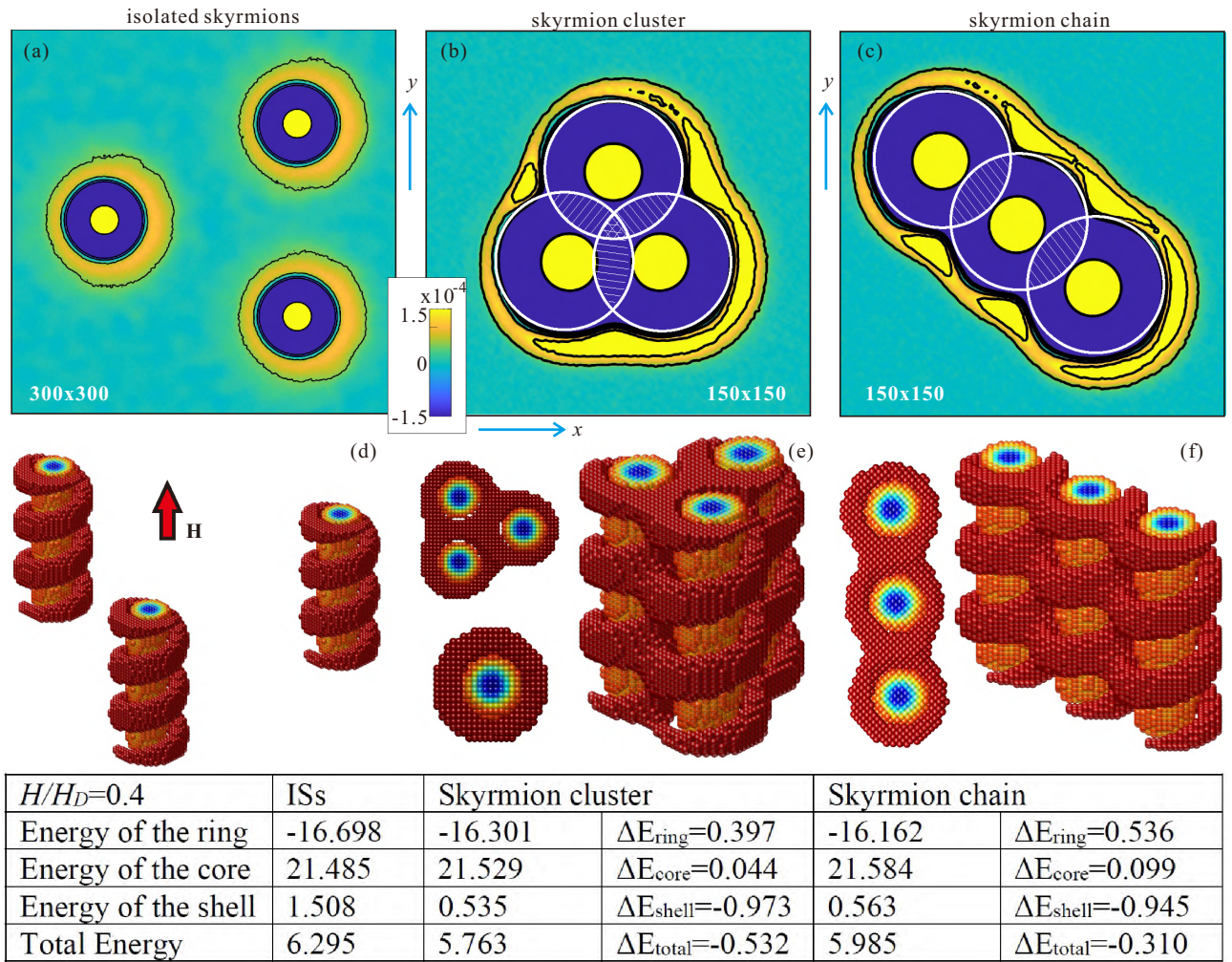


FIG. 3. The color plots of the energy density averaged over  $z$  coordinates and plotted on the  $xy$  plane for three distinct configurations: isolated skyrmions (a), trio-clusters (b), and trio-chains (c). The white circles in (b) and (c) show the boundaries of the skyrmion rings. Thus, within the hatched areas, skyrmion clusters and chains compromise some negative energy of the rings to eradicate simultaneously the positive energy of the shells. The table exhibits the energetic balance within different skyrmion structures and indicates that skyrmion clusters are the most energetically favorable configurations. Corresponding 3D constructs in (d)–(f) exhibit the way the coils of constituent skyrmions are getting “zipped” together. In this case, the size of a numerical grid along  $z$  equals  $\lambda$ , and periodic boundary conditions are used. In (d)–(f), the size along  $z$  is  $3\lambda$ .

by de Gennes [53] for (continuous) transitions into incommensurate modulated phases. According to de Gennes, the fully saturated ferromagnetic state is stable locally. However, it becomes unstable with respect to certain distortions of large-amplitude skyrmions: in practice, isolated skyrmions as excitations of a ferromagnetic state nucleate near defects, and then they condense into the lattice. Such nucleation-type phase transitions are rather frequent in condensed-matter physics: (a) the entry of magnetic flux in a type II superconductors involves nucleation of vortex lines; (b) an electric or magnetic field induces the transition between a cholesteric and a nematic liquid crystal; (c) the magnetic samples break up into domains with an increasing role of the demagnetizing field. And vice versa, the magnetic state built up from skyrmions may be decomposed into an assembly of isolated skyrmion-molecular units, i.e., a transformation of condensed phases occurs by setting free the isolated skyrmion units as in

a crystal-gas resublimation. Depending on small energy differences due to additional effects, different extended textures with variable arrangements of the skyrmion cores may arise, just as in a molecular crystal.

## V. ISOLATED SKYRMIONS IN THIN FILMS OF CUBIC HELIMAGNETS

To reveal the mechanism of skyrmion cluster formation in thin films, we first limit ourselves by the thickness range  $\nu < \lambda$ . The energy profiles induced by the surface twists are plotted in Fig. 4 and are markedly different from those for bulk helimagnets in Fig. 2(a). Moreover, the energetic pattern changes while penetrating into the depth of a sample [Fig. 4(a)], and only for  $z = \lambda/2$  does it become similar to a motif with clearly distinguishable core and crescent parts. Superposition of all energy profiles from the lower [first panel



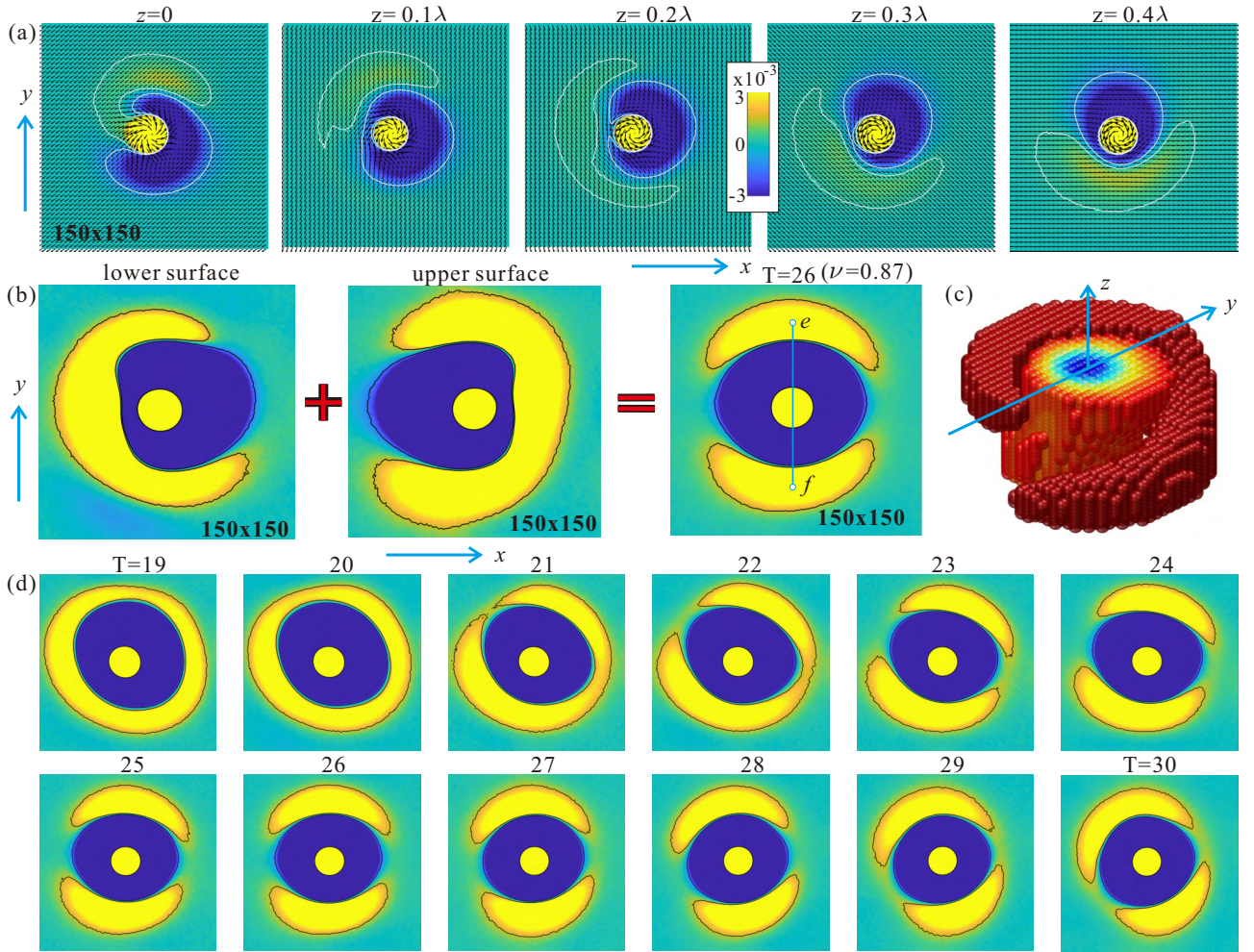


FIG. 4. (a) Energy density distributions plotted on the plane  $xy$  while going from the lower film surface [first panel in (a) at  $z = 0$ ] into the depth of the layer. Manifested transformation of the energy profiles is directly related to the surface twists, which become apparent in the in-plane magnetization rotation toward the surfaces. At the penetration depth  $z = \lambda/2$ , the energy pattern becomes similar to the one for bulk helimagnets in Fig. 2(a). (b) Superposition of average energy profiles from the lower (first panel) and upper (second panel) surfaces results in the total polar energy pattern (third panel), in which the bags of the positive energy density (not the circular shell, as was discovered for bulk helimagnets in Fig. 2) are located along the line  $e - f$ . (c) 3D skyrmion model, which corresponds to the described energy profiles and exhibits only a patch of the coil around the skyrmion core. Such an internal skyrmion structure implies the formation of skyrmion chains rather than clusters (see the text for details). (d) A thickness-dependent evolution of average energy profiles, which mainly indicates their polar nature (from  $T = 21$  to 30), although for smaller thicknesses the energy patterns become circular.

in Fig. 4(b) and upper [second panel in Fig. 4(b)] surfaces leads to a characteristic resulting profile with two bags of positive energy density located along the line  $e - f$  (the points  $e$  and  $f$  are the centers of two crescents). The same energy profile holds in a range of thicknesses as shown by Fig. 4(d) and implies skyrmion chain formation rather than skyrmion clusters. Indeed, the most effective elimination of the positive energy density of skyrmion shells must be achieved if isolated skyrmions line up into a chain. In addition to the energy arguments, a 3D model of a skyrmion [Fig. 4(c)] vividly reveals that the compact skyrmion chain must be formed along the  $y$  axis [as depicted in Fig. 5(b)].

And indeed, for  $\nu = 0.87$  ( $T = 26$ ), the skyrmion trio-chain has smaller total energy (see the table in Fig. 5) as compared with the skyrmion trio-cluster composed of three skyrmions [Figs. 5(a)–5(d)]. Such a chain configuration virtually eradicates the shell in the interskyrmion region. Only

small roundish parts numbered  $a_1 - a_4$  in Fig. 5(a) remain. Although the chain configuration significantly “loses” energy in the ring, the total energy gain

$$\Delta E = \Delta E_{\text{ring}} + \Delta E_{\text{shell}} \quad (10)$$

makes it a better configuration than the corresponding cluster [Fig. 5(c)]. The cluster being effective in preserving the ring energy, however, is unable to suppress the shell energy, and vast areas of the positive energy density still exist around the cluster configuration. I also notice that the constituent skyrmions within both configurations appear distorted. They significantly increase the positive energy of their cores. Moreover, the skyrmion rings exhibit some ellipticity. At the same time, the total energy of skyrmions in all configurations is negative as compared with the energy of the conical phase. It becomes positive at  $\nu = 1.41$  (for isolated skyrmions),  $\nu = 1.46$  (for skyrmion trio-chains), and  $\nu = 1.50$  (for skyrmion

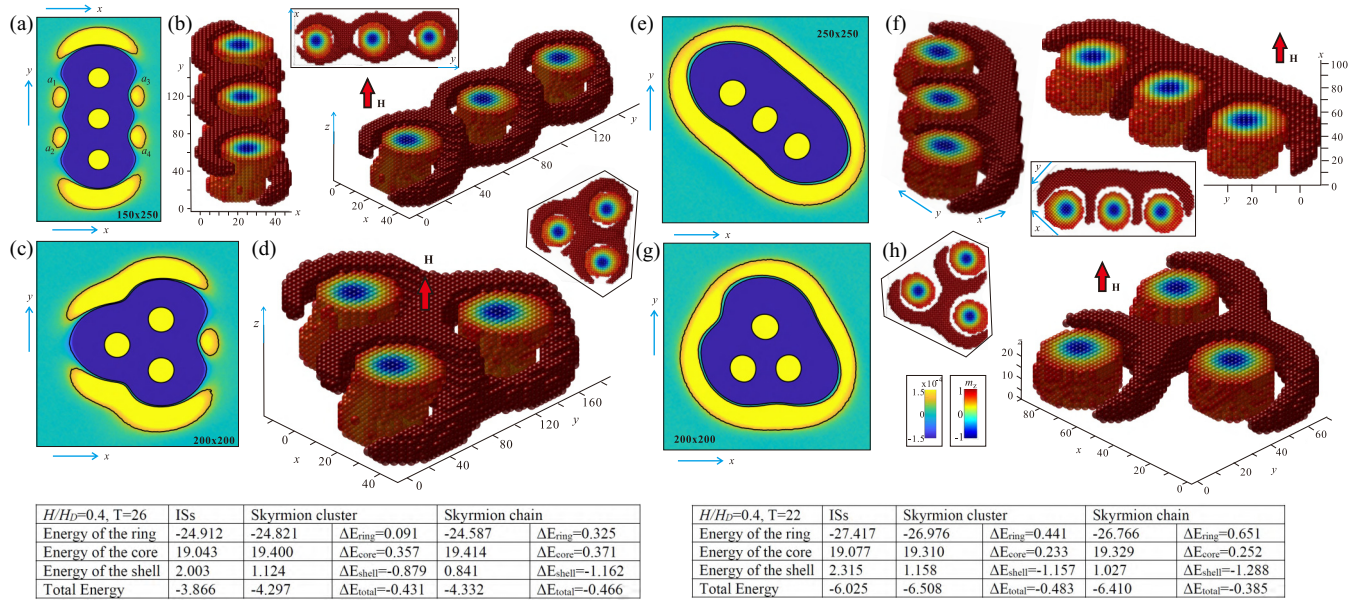


FIG. 5. The internal structure of skyrmion trio-clusters and trio-chains for two different thicknesses of the film:  $T = 26$  (a)–(d) and  $T = 22$  (e)–(h). Corresponding tables show the energy balance within the skyrmion conglomerates in the same way as was previously done for skyrmions in bulk helimagnets. For pronouncedly polar energy distributions (for  $T = 26$ ), the advantage of skyrmion chains is manifested by the effective suppression of skyrmion shells. Only small remainders  $a_1 - a_4$  of the shells are still maintained aside from the polar axis of the trio-chain (a). The trio-clusters (b) in this case are less effective in the shell eradication. 3D constructs also exhibit compact zipping of skyrmion loops within the trio-chains (b) and trio-clusters (d). For  $T = 22$ , the more prolonged shell underlies the advantage of skyrmion trio-clusters. In both cases, the shell surrounds the resulting skyrmion conglomerates.

trio-clusters). By adding more skyrmions into a skyrmion cluster, this critical thickness value gradually increases until it reaches a much higher value for the hexagonal SkL [33,43]. Initially, this fact motivated the omission of the region of the stable SkL at the phase diagram [Fig. 1(a)].

Remarkably, the same energetic reasoning does not lead to the chain advantage at  $\nu = 0.73$  [Figs. 5(e)–5(h)]. In the same way, the chain more effectively eradicates the shell and loses some energy of the ring, however the total energy balance (10) implies the preference of a skyrmion cluster. The reason presumably lies in the more extended shell for  $\nu = 0.73$  as opposed to the more concentrated polar shell at  $\nu = 0.87$ . In this case, the cluster eliminates the shell energy almost as effectively as is done in chains, but with the lower loss of the ring energy it comes out with a lower total energy. The exhaustive field- and thickness-dependent analysis of skyrmion clusters and chains will be done elsewhere. The present speculations, however, imply that the mechanism of cluster formation rests on an intricate balance of energy contributions stored in separate parts of a nonaxisymmetric skyrmion. The analysis will become even more complicated for thicker films, since in this case uncompensated bulk energy profiles [inset in Fig. 2(i)] will admix and possibly lead to anisotropic effects and predefined configurations of skyrmion clusters and chains.

## VI. CONCLUSIONS

To conclude, I have examined the properties of nonaxisymmetric skyrmions within the conical state and the mechanism

leading to their attraction in bulk and thin-layered cubic helimagnets. The analysis is based on the scrutiny of energy profiles both in an individual cross-section  $xy$  for a fixed coordinate  $z$  and averaged over some distance along the  $z$  axis, i.e., over the cone period and/or the film thickness. A characteristic feature of the energy patterns is a shell region with positive energy density, which encompasses isolated skyrmions and can be thought of as the domain boundary between the conical phase and isolated skyrmions due to their incompatibility. It was shown that the metastable skyrmions in bulk helimagnets develop the tendency to gather into “crowds,” and by this to reduce the shell energy, although at some expense of the negative energy of skyrmion rings, i.e., the energy balance  $\Delta E_{\text{ring}} + \Delta E_{\text{shell}}$  defines the geometry of a skyrmion group. Since the shell energy is homogeneous around a skyrmion, the cluster obviously constitutes the most energetically favorable skyrmion conglomerate. In thin layers, however, the shell is mostly related to the magnetization surface twists and exhibits the polar pattern with two positive bags on two opposite sides from the skyrmion center. In this case, individual skyrmions prefer to align into a “queue” to effectively eradicate the positive bags in the interskyrmion region. A systematic analysis of skyrmion trio-clusters and trio-chains showed that although the same energy balance between the “lost” negative energy of the skyrmion rings and the “gained” energy due to the suppressed shells comes into play, the tendency to form either clusters or chains changes with the film thickness. Thus, the results of the present manuscript also pose new questions about topological and energetic properties of clusters and chains composed from the higher number of isolated skyrmions. In particular, for four skyrmions, one

would infer a considerably larger inventory of possibilities to form skyrmion conglomerates, which would include also their square arrangement. Remarkably, the concepts of cluster formation in chiral magnets are readily applicable to chiral liquid crystals. In fact, the polar ordering of nonaxisymmetric skyrmions was recently observed experimentally within the “schools” of liquid-crystal skyrmions moved by an applied electric field [30,31]. Moreover, I identified a low-field spiral state that serves as a buffer state between the conventional cones and helicoids and is stable in a broad parameter range at the phase diagram. Such an oblique spiral constitutes an interesting deviation from the previously published phase diagrams for thin-film helimagnets, which may have important

consequences for the field of chiral magnetism. In particular, the spiral tilt can also give rise to new topological magnetic defects, such as isolated skyrmions, with interesting static and dynamic properties.

## ACKNOWLEDGMENTS

I am grateful to Ivan Smalyukh, Ulrich Röbler, Katia Pappas, Natsuki Mukai, and Kaito Tsunoki for useful discussions. I also thank Ulrike Nitzsche for technical assistance, and acknowledge JSPS Grant-in-Aid (C) 21K03406.

- 
- [1] A. N. Bogdanov and D. A. Yablonsky, Thermodynamically stable vortices in magnetically ordered crystals. Mixed state of magnetics, *Zh. Eksp. Teor. Fiz.* **95**, 178 (1989) [*Sov. Phys. JETP* **68**, 101 (1989)].
- [2] N. Nagaosa and Y. Tokura, Topological properties and dynamics of magnetic skyrmions, *Nat. Nanotechnol.* **8**, 899 (2013).
- [3] *Magnetic Skyrmions and Their Applications*, edited by G. Finocchio and C. Panagopoulos (Woodhead, Cambridge, UK, 2020).
- [4] T. Moriya, Anisotropic superexchange interaction and weak ferromagnetism, *Phys. Rev.* **120**, 91 (1960).
- [5] I. E. Dzyaloshinskii, Theory of helicoidal structures in antiferromagnets. I. Nonmetals, *J. Sov. Phys. JETP-USSR* **19**, 960 (1964); The theory of helicoidal structures in antiferromagnets. II. Metals, **20**, 223 (1965).
- [6] S. Mühlbauer, B. Binz, F. Jonietz, C. Pfleiderer, A. Rosch, A. Neubauer, R. Georgii, P. Böni, Skyrmion lattice in a chiral magnet, *Science* **323**, 915 (2009).
- [7] H. Wilhelm, A. O. Leonov, U. K. Rossler, P. Burger, F. Hardy, C. Meingast, M. E. Gruner, W. Schnelle, M. Schmidt, and M. Baenitz, Scaling study and thermodynamic properties of the cubic helimagnet FeGe, *Phys. Rev. B* **94**, 144424 (2016).
- [8] A. Bogdanov and A. Hubert, Thermodynamically stable magnetic vortex states in magnetic crystals, *J. Magn. Magn. Mater.* **138**, 255 (1994); The stability of vortex-like structures in uniaxial ferromagnets, **195**, 182 (1999).
- [9] R. H. Hobart, On the instability of a class of unitary field models, *Proc. Phys. Soc. London* **82**, 201 (1963); G. H. Derrick, Comments on nonlinear wave equations as models for elementary particles, *J. Math. Phys.* **5**, 1252 (1964).
- [10] E. M. R. Tomasello, R. Zivieri, L. Torres, M. Carpentieri, and G. Finocchio, A strategy for the design of skyrmion racetrack memories, *Sci. Rep.* **4**, 6784 (2014).
- [11] J. Müller, Magnetic skyrmions on a two-lane racetrack, *New J. Phys.* **19**, 025002 (2017).
- [12] W. Kang, Y. Huang, C. Zheng, W. Lv, Na Lei, Y. Zhang, X. Zhang, Y. Zhou, and W. Zhao, Voltage controlled magnetic skyrmion motion for racetrack memory, *Sci. Rep.* **6**, 23164 (2016).
- [13] A. Fert, V. Cros, and J. Sampaio, Skyrmions on the track, *Nat. Nanotechnol.* **8**, 152 (2013).
- [14] X. Z. Yu, Y. Onose, N. Kanazawa, J. H. Park, J. H. Han, Y. Matsui, N. Nagaosa, and Y. Tokura, Real-space observation of a two-dimensional skyrmion crystal, *Nature* **465**, 901 (2010).
- [15] X. Z. Yu, N. Kanazawa, Y. Onose, K. Kimoto, W. Z. Zhang, S. Ishiwata, Y. Matsui, and Y. Tokura, Near room-temperature formation of a skyrmion crystal in thin-films of the helimagnet FeGe, *Nat. Mater.* **10**, 106 (2011).
- [16] J. C. Loudon, A. O. Leonov, A. N. Bogdanov, M. C. Hatnean, and G. Balakrishnan, Direct observation of attractive skyrmions and skyrmion clusters in the cubic helimagnet Cu<sub>2</sub>OSeO<sub>3</sub>, *Phys. Rev. B* **97**, 134403 (2018).
- [17] H. Du, X. Zhao, F. N. Rybakov, A. B. Borisov, S. Wang, J. Tang, C. Jin, C. Wang, W. Wei, N. S. Kiselev, Y. Zhang, R. Che, S. Blügel, and M. Tian, Interaction of Individual Skyrmions in a Nanostructured Cubic Chiral Magnet, *Phys. Rev. Lett.* **120**, 197203 (2018).
- [18] H. R. O. Sohn, S. M. Vlasov, V. M. Uzdin, A. O. Leonov, and I. I. Smalyukh, Real-space observation of skyrmion clusters with mutually orthogonal skyrmion tubes, *Phys. Rev. B* **100**, 104401 (2019).
- [19] D. Foster, C. Kind, P. J. Ackerman, J.-S. B. Tai, M. R. Dennis, and I. I. Smalyukh, Two-dimensional skyrmion bags in liquid crystals and ferromagnets, *Nat. Phys.* **15**, 655 (2019).
- [20] A. O. Leonov and C. Pappas, Skyrmion clusters and conical droplets in bulk helimagnets with cubic anisotropy, *Phys. Rev. B* **99**, 144410 (2019).
- [21] P. Oswald and P. Pieranski, *Nematic and Cholesteric Liquid Crystals: Concepts and Physical Properties Illustrated by Experiments* (CRC, Boca Raton, FL, 2005).
- [22] M. Kleman and O. D. Lavrentovich, *Soft Matter Physics: An Introduction* (Springer-Verlag, New York, 2003).
- [23] P. J. Ackerman and I. I. Smalyukh, Diversity of knot solitons in liquid crystals manifested by linking of preimages in torons and hopfions, *Phys. Rev. X* **7**, 011006 (2017).
- [24] I. I. Smalyukh, Y. Lansac, N. Clark, and R. Trivedi, Three-dimensional structure and multistable optical switching of triple-twisted particle-like excitations in anisotropic fluids, *Nat. Mater.* **9**, 139 (2010).
- [25] P. J. Ackerman and I. I. Smalyukh, Static three-dimensional topological solitons in fluid chiral ferromagnets and colloids, *Nat. Mater.* **16**, 426 (2016).

- [26] S. D. Hudson and E. L. Thomas, Disclination interaction in an applied field: Stabilization of the Lehmann cluster, *Phys Rev A* **44**, 8128 (1991).
- [27] I. I. Smalyukh, Review: Knots and other new topological effects in liquid crystals and colloids, *Rep. Prog. Phys.* **83**, 106601 (2020).
- [28] J.-S. B. Tai and I. I. Smalyukh, Surface anchoring as a control parameter for stabilizing torons, skyrmions, twisted walls, fingers, and their hybrids in chiral nematics, *Phys. Rev. E* **101**, 042702 (2020).
- [29] M. T. Birch, D. Cortes-Ortuno, N. D. Khanh, S. Seki, A. Stefancic, G. Balakrishnan, Y. Tokura, and P. D. Hatton, Topological defect-mediated skyrmion annihilation in three dimensions, *Commun. Phys.* **4**, 175 (2021).
- [30] H. R. O. Sohn, C. D. Liu, and I. I. Smalyukh, Schools of skyrmions with electrically tunable elastic interactions, *Nat. Commun.* **10**, 4744 (2019).
- [31] H. R. O. Sohn, C. D. Liu, Y. Wang, and I. I. Smalyukh, Light-controlled skyrmions and torons as reconfigurable particles, *Opt. Express* **27**, 29056 (2019).
- [32] F. N. Rybakov, A. B. Borisov, and A. N. Bogdanov, Three-dimensional skyrmion states in thin films of cubic helimagnets, *Phys. Rev. B* **87**, 094424 (2013).
- [33] A. O. Leonov, Y. Togawa, T. L. Monchesky, A. N. Bogdanov, J. Kishine, Y. Kousaka, M. Miyagawa, T. Koyama, J. Akimitsu, Ts. Koyama, K. Harada, S. Mori, D. McGrouther, R. Lamb, M. Krajnak, S. McVitie, R. L. Stamps, and K. Inoue, Chiral Surface Twists and Skyrmion Stability in Nanolayers of Cubic Helimagnets, *Phys. Rev. Lett.* **117**, 087202 (2016).
- [34] D. Suess, C. Vogler, F. Bruckner, P. Heistracher, and C. Abert, A repulsive skyrmion chain as a guiding track for a racetrack memory, *AIP Adv.* **8**, 115301 (2018).
- [35] D. Capic, D. A. Garanin, and E. M. Chudnovsky, Skyrmion-skyrmion interaction in a magnetic film, *J. Phys.: Condens. Matter* **32**, 415803 (2020).
- [36] A. O. Leonov, T. L. Monchesky, N. Romming, A. Kubetzka, A. N. Bogdanov, and R. Wiesendanger, The properties of isolated chiral skyrmions in thin magnetic films, *New J. Phys.* **18**, 065003 (2016).
- [37] P. J. Ackerman, T. Boyle, and I. I. Smalyukh, Squirring motion of baby skyrmions in nematic fluids, *Nat. Commun.* **8**, 673 (2017).
- [38] P. Bak and M. H. Jensen, Theory of helical magnetic structures and phase transitions in MnSi and FeGe, *J. Phys. C* **13**, L881 (1980).
- [39] A. O. Leonov, Surface anchoring as a control parameter for shaping skyrmion or toron properties in thin layers of chiral nematic liquid crystals and noncentrosymmetric magnets, *Phys Rev E* **104**, 044701 (2021).
- [40] A. O. Leonov, C. Pappas, and I. I. Smalyukh, Field-driven metamorphoses of isolated skyrmions within the conical state of cubic helimagnets, *Phys. Rev. B* **104**, 064432 (2021).
- [41] A. O. Leonov, T. L. Monchesky, J. C. Loudon, and A. N. Bogdanov, Three-dimensional chiral skyrmions with attractive interparticle interactions, *J. Phys.: Condens. Matter* **28**, 35LT01 (2016).
- [42] A. O. Leonov, J. C. Loudon, and A. N. Bogdanov, Spintronics via non-axisymmetric skyrmions, *Appl. Phys. Lett.* **109**, 172404 (2016).
- [43] F. N. Rybakov, A. B. Borisov, S. Bluegel, and N. S. Kiselev, New spiral state and skyrmion lattice in 3D model of chiral magnets, *New J. Phys.* **18**, 045002 (2016).
- [44] A. O. Leonov, I. M. Tambovtcev, I. S. Lobanov, and V. M. Uzdin, Stability of in-plane and out-of-plane chiral skyrmions in epitaxial MnSi (111)/Si (111) thin films: Surface twists versus easy-plane anisotropy, *Phys. Rev. B* **102**, 174415 (2020).
- [45] E. A. Karhu, U. K. Röbber, A. N. Bogdanov, S. Kahwaji, B. J. Kirby, H. Fritzsche, M. D. Robertson, C. F. Majkrzak, and T. L. Monchesky, *Phys. Rev. B* **85**, 094429 (2012).
- [46] I. I. Smalyukh, B. I. Senyuk, P. Palfy-Muhoray, O. D. Lavrentovich, H. Huang, E. C. Gartland, V. H. Bodnar, T. Kosa, and B. Taheri, Electric-field-induced nematic-cholesteric transition and three-dimensional director structures in homeotropic cells, *Phys. Rev. E* **72**, 061707 (2005).
- [47] D. McGrouther, R. J. Lamb, M. Krajnak, S. McFadzean, S. McVitie, R. L. Stamps, A. O. Leonov, A. N. Bogdanov, and Y. Togawa, Internal structure of hexagonal skyrmion lattices in cubic helimagnets, *New J. Phys.* **18**, 095004 (2016).
- [48] M. T. Birch, D. Cortés-Ortuño, L. A. Turnbull, M. N. Wilson, F. Groß, N. Träger, A. Laurensen, N. Bukin, S. H. Moody, M. Weigand, G. Schütz, H. Popescu, R. Fan, P. Steadman, J. A. T. Verezhak, G. Balakrishnan, J. C. Loudon, A. C. Twitchett-Harrison, O. Hovorka, H. Fangohr, F. Y. Ogrin, J. Gräfe, *et al.*, Real-space imaging of confined magnetic skyrmion tubes, *Nat. Commun.* **11**, 1726 (2020).
- [49] D. Wolf, S. Schneider, U. K. Röbber, A. Kovacs, M. Schmidt, R. E. Dunin-Borkowski, B. Büchner, B. Rellinghaus, and A. Lubk, Unveiling the three-dimensional spin texture of skyrmion tubes, [arXiv:2101.12630](https://arxiv.org/abs/2101.12630).
- [50] S. Schneider, D. Wolf, M. J. Stolt, S. Jin, D. Pohl, B. Rellinghaus, M. Schmidt, B. Büchner, S. T. B. Goennenwein, K. Nielsch, and A. Lubk, Induction Mapping of the 3D-Modulated Spin Texture of Skyrmions in Thin Helimagnets, *Phys. Rev. Lett.* **120**, 217201 (2018).
- [51] A. B. Butenko, A. A. Leonov, U. K. Röbber, and A. N. Bogdanov, Stabilization of skyrmion textures by uniaxial distortions in noncentrosymmetric cubic helimagnets, *Phys. Rev. B* **82**, 052403 (2010).
- [52] A. Hubert and R. Schäfer, *Magnetic Domains* (Springer, Berlin, 1998).
- [53] P. G. de Gennes, in *Fluctuations, Instabilities, and Phase Transitions*, edited by T. Riste, Vol. 2 of NATO Advanced Study Institute Series B: Physics (Plenum, New York, 1975).